


Acoustic metamaterials with spinning componentsDegang Zhao,^{1,2,*} Yao-Ting Wang,^{2,3,4,*} Kin-Hung Fung⁵, Zhao-Qing Zhang,² and C. T. Chan^{2,†}¹*School of Physics, Huazhong University of Science and Technology, Wuhan 430074, China*²*Department of Physics, The Hong Kong University of Science and Technology, Clear Water Bay, Hong Kong, China*³*Department of Physics, Imperial College London, London SW7 2AZ, United Kingdom*⁴*School of Physics and Astronomy, The University of Birmingham, Birmingham B15 2TT, United Kingdom*⁵*Department of Applied Physics, The Hong Kong Polytechnic University, Hong Kong, China*

(Received 21 June 2019; revised manuscript received 27 January 2020; accepted 29 January 2020; published 12 February 2020)

We show that an acoustic metamaterial consisting of an array of spinning cylindrical inclusions can possess many unusual properties, including folded bulk bands and interface-state bands. The folding of bands inside the first Brillouin zone is made possible by a rotation-induced antiresonance of compressibility and the rotational Doppler effect. Both bulk and interface-state band dispersions exhibit remarkable filling-fraction-dependent features such as the emergence of a cutoff frequency when the filling fraction exceeds a critical value. Robust one-way transport properties are supported by nondegenerate interface states, but within the same band, interface states at different frequencies can have different propagation directions.

DOI: [10.1103/PhysRevB.101.054107](https://doi.org/10.1103/PhysRevB.101.054107)**I. INTRODUCTION**

Acoustic metamaterials (AMs) are artificial acoustic composites made of subwavelength microstructures, and they exhibit novel wave phenomena or functionalities not found in natural acoustic materials. Exotic examples of these phenomena include acoustic superlenses [1–3], invisibility cloaks [4–8], acoustic black holes [9–13], and topological acoustic materials [14–19]. One of the most striking properties of AMs is the negative effective constitutive parameters in low frequencies. For example, negative mass density can be achieved by a composite consisting of heavy metal beads coated in soft rubber [20,21], while negative bulk modulus can be achieved by a periodic array of Helmholtz resonators [22]. Subsequently, various AMs simultaneously possessing negative mass density and negative bulk modulus have been proposed [23–26]. If one allows relative motion between the constituent materials in AMs, the additional degrees of freedom due to kinetic equilibrium can give rise to even more interesting phenomena. As noted by Censor *et al.* [27], sound waves can be scattered by an isotropic scatterer rotating at a constant angular velocity even if the inclusion and the background medium are identical. Their results imply that the rotation of the scatterer can dramatically transform the acoustic properties of an AM. Furthermore, the assumption of rotation of inclusions implicitly implies the existence of interactions between the system and the environment driving the inclusions at a prespecified angular velocity. The system is in fact non-Hermitian. Recently, the non-Hermitian acoustic system has attracted much attention thanks to its many unique properties that are absent in conventional Hermitian systems [14–19,28–30].

In this work, we study both the bulk and interface-state bands of AM consisting of spinning cylindrical inclusions using multiple scattering theory (MST) [31,32] as well as effective-medium theory (EMT) [33]. Both bulk and interface-state bands exhibit interesting band-folding behaviors in the subwavelength realm. Due to the band folding inside the first Brillouin zone, there are sets of k -points that carry no real eigenvalues. Consequently, gaps are “horizontally” opened in momentum space in the Brillouin zone [34]. Such gaps are sometimes referred to as “ k -gaps” and they have been found in non-Hermitian systems [35–40]. We note that these k -gaps do not appear in Hermitian topological phononic crystals, and in our system they are induced by the spinning of the cylindrical inclusions. The effective compressibility shows that a rotation-induced antiresonance behavior [41], together with the rotational Doppler effect, which breaks the chiral symmetry of the effective-mass densities, leads to the formation of the folded bulk and interface-state bands. The interface states are unidirectional and can have opposite propagating directions within the same band because the interface bands can fold within the first Brillouin zone. This unusual phenomenon cannot occur in Hermitian topological crystals. Their robust one-way transport is numerically demonstrated. The evolutions of bulk and interface-state bands are systematically analyzed by varying the filling fraction f of the spinning cylinders in the lattice. We find that the band dispersion can change dramatically when the filling fraction is varied. This rotation-induced dispersion enables us to realize a new class of AM without introducing any resonant element.

II. DISPERSION RELATION OF BULK BANDS AND EFFECTIVE-MEDIUM DESCRIPTION

We begin by considering a two-dimensional (2D) periodic array of fluid cylinders, with mass density ρ_s and acoustic

*These authors contributed equally to this work.

†Corresponding author: phchan@ust.hk

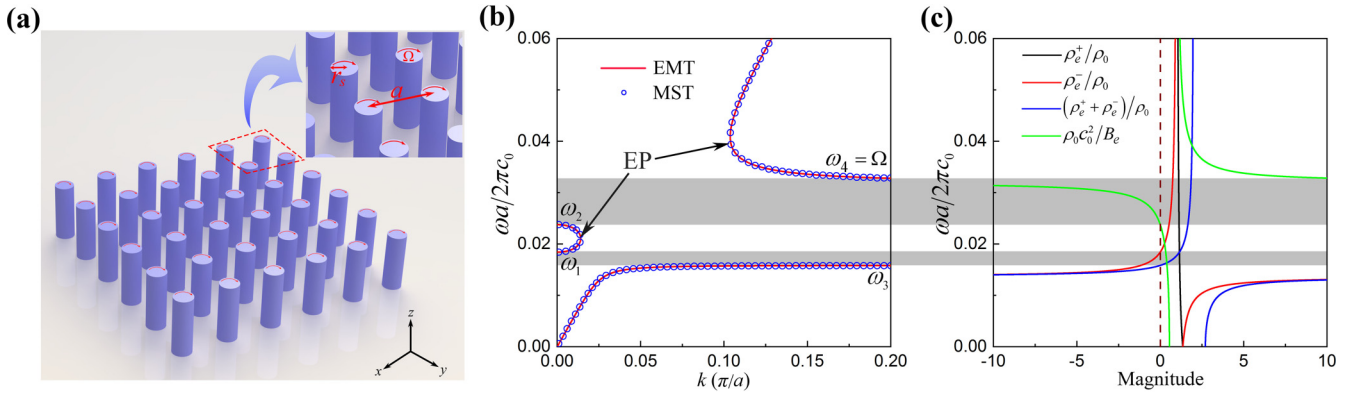


FIG. 1. (a) A two-dimensional square array of rotating cylinders in a fluidic background. Each cylinder rotates about its symmetric axis at a constant angular velocity Ω . (b) The band structures calculated by MST and EMT at a filling ratio $f = 0.15$ showing two rotation-induced gaps (shaded in gray) sandwiching a “folded” band in between. The bands intercept the Brillouin zone center and boundaries at ω_1 , ω_2 , ω_3 , and ω_4 . (c) Effective-mass densities and compressibility vs frequencies at $f = 0.15$.

wave velocity c_s , immersed in a fluidic background with mass density ρ_0 and acoustic wave velocity c_0 , as shown in Fig. 1(a). We assume that the rotating fluid inclusions are contained in a very thin stationary solid shell, which separates the spinning fluid from the static background so that they will not mix, and we will take the limit that the solid wall is so thin such that the pressure and the radial displacement are continuous across the boundary. The lattice constant is a , the radius of cylinders is r_s , and each cylinder rotates about its symmetric z axis at a uniform angular velocity Ω , which is defined as positive (negative) for anticlockwise (clockwise) rotation. While Fig. 1(a) illustrates a square lattice of cylinders, the lattice symmetry is in fact immaterial because we are interested in the low-frequency regime where the lattice can be viewed as a homogenized medium. For simplicity, we ignore the viscosity of the fluids in our theoretical analysis. In polar coordinates, the radial component of the pressure acoustic wave equation inside the inclusion is given by [27]

$$r^2 \partial_r^2 p + r \partial_r p + (r^2 \lambda_m^2 - m^2) p = 0, \quad (1)$$

where p is the pressure; m is the integer angular index, which yields $\partial_\theta p = i m p$; and $\lambda_m^2 = -(4\Omega^2 + M^2) c_s^{-2}$ gives the rotating wave number λ_m . The frequency correction $M = -i(\omega - m\Omega)$ arises from the rotational Doppler effect [42] that causes frequency shifts of waves propagating from static to rotating media and breaks the symmetry between m and $-m$ states. Outside the inclusion, Eq. (1) is replaced by

$$r^2 \partial_r^2 p + r \partial_r p + (r^2 k_0^2 - m^2) p = 0, \quad (2)$$

where $k_0 = \omega/c_0$ denotes the wave number in the background medium. The general solutions of Eqs. (1) and (2) have the forms $p_{\text{in}} = \sum_{m=-\infty}^{\infty} a_m J_m(\lambda_m r) e^{im\theta}$ inside the inclusion and $p_{\text{out}} = \sum_{m=-\infty}^{\infty} b_m J_m(k_0 r) e^{im\theta} + c_m H_m(k_0 r) e^{im\theta}$ outside the inclusion. Here $J_m(x)$ and $H_m(x)$ are the Bessel function and Hankel function of the first kind, respectively. To match the boundary conditions, we further need the radial displacements u_r inside the inclusion, which has the form [27]

$$u_r = [(2\Omega^2 - M^2) \partial_r p - 3imM\Omega p / r] \times [\rho_s (M^2 + 4\Omega^2) (M^2 + \Omega^2)]. \quad (3)$$

After applying the boundary conditions that both p and u_r are continuous at $r = r_s$, the Mie scattering coefficients can be obtained as [27]

$$D_m = -\frac{\lambda_m \rho_0 R_m(\lambda_m r_s) J_m(k_0 r_s) - k_0 \rho_s J_m(\lambda_m r_s) J'_m(k_0 r_s)}{\lambda_m \rho_0 R_m(\lambda_m r_s) H_m(k_0 r_s) - k_0 \rho_s J_m(\lambda_m r_s) H'_m(k_0 r_s)}, \quad (4)$$

where

$$R_m(\lambda_m r_s) = \frac{\omega^2}{(4\Omega^2 + M^2)(\Omega^2 + M^2)} \times \left[(2\Omega^2 - M^2) J'_m(\lambda_m r_s) - 3imM\Omega \frac{J_m(\lambda_m r_s)}{\lambda_m r_s} \right]. \quad (5)$$

Equation (4) describes the scattering of a single rotating cylinder. This equation enables us to calculate the band structures by using MST [31,32] in any frequency range.

Knowing the Mie scattering coefficients D_m , we can obtain the effective-medium parameters in the long-wavelength regime. Using the EMT technique [33], we obtain the following effective bulk modulus B_e and effective-mass densities ρ_e^\pm from D_0 and $D_{\pm 1}$, respectively (see Appendix A for details):

$$B_e^{-1} = f B_{es}^{-1} + (1-f) B_0^{-1} \quad \text{with} \quad B_{es}^{-1} = \frac{2\Omega^2 + \omega^2}{\rho_s c_s^2 (\omega^2 - \Omega^2)},$$

$$\rho_e^\pm = \rho_0 \frac{(1+f)\rho_{es}^\pm + (1-f)\rho_0}{(1-f)\rho_{es}^\pm + (1+f)\rho_0} \quad \text{with} \quad \rho_{es}^\pm = \rho_s \left(1 \pm \frac{\Omega}{\omega} \right), \quad (6)$$

where f denotes the filling fraction of the cylinders and the \pm sign refers to anticlockwise/clockwise rotation (“ $m = \pm 1$ ”). B_{es} and ρ_{es}^\pm are, respectively, the effective bulk modulus and effective-mass densities of the spinning cylinders seen in the laboratory frame. The B_{es} and ρ_{es}^\pm expressions can also be independently derived from the scattering of a single spinning cylinder [see Eqs. (B14), (B15), and (C5) in the Appendixes]. The splitting of ρ_e^+ and ρ_e^- (or ρ_{es}^+ and ρ_{es}^-) is a result of the rotational Doppler effect, which makes $D_1 \neq D_{-1}$. Equation (6) indicates that an ordinary material

that has a frequency-independent response can be turned into a dispersive medium when parts of the medium are spinning. In addition, transforming the density terms in Eq. (6) into Cartesian coordinates in the x - y plane leads to an anisotropic density tensor of the form (see Appendix B for details)

$$\vec{\rho}_e = \frac{1}{2} \begin{pmatrix} \rho_e^+ + \rho_e^- & -i(\rho_e^+ - \rho_e^-) \\ i(\rho_e^+ - \rho_e^-) & \rho_e^+ + \rho_e^- \end{pmatrix}. \quad (7)$$

By substituting B_e and $\vec{\rho}_e$ into the acoustic wave equation

$$B_e \nabla (\nabla \cdot \vec{v}) = \vec{\rho}_e \frac{\partial^2 \vec{v}}{\partial t^2}, \quad (8)$$

we obtain the following effective-medium dispersion relation:

$$k^2 = \frac{2\omega^2 \rho_e^+ \rho_e^-}{(\rho_e^+ + \rho_e^-) B_e}. \quad (9)$$

As an example, we consider a system in which the rotating cylinders and the background medium are both water ($\rho_0 = \rho_s = 1000 \text{ kg/m}^3$, $c_0 = c_s = 1490 \text{ m/s}$) and we set $a = 0.1 \text{ m}$, $f = 0.15$, and $\Omega = 3000 \text{ rad/s}$. The band structures calculated using MST and EMT are compared in Fig. 1(b). The excellent agreement between the EMT and MST results confirms the validity of Eq. (9). It is interesting to find that even though the inclusion and the background medium are identical, two rotation-induced band gaps emerge in the low-frequency regime with a folded band lying in between. The physics of these resonant gaps and the folded band can be understood from the effective parameters depicted in Fig. 1(c). According to Eq. (9), a band gap occurs if its right-hand side is negative, which is determined by the signs of B_e^{-1} , ρ_e^+ , ρ_e^- , and $\rho_e^+ + \rho_e^-$. Figure 1(c) clearly indicates that the first band gap stems from the single negativity of ρ_e^- . The second band gap originates from the negativity of the effective compressibility B_e^{-1} arising from the antiresonance of B_e^{-1} at $\omega = \Omega$ as the frequency dependence of the response function B_e^{-1} exhibits an opposite trend to that of ρ_e^- [41]. Thus, the presence of antiresonance in B_e^{-1} , together with the rotational Doppler effect which breaks the symmetry between ρ_e^+ and ρ_e^- , produces such a unique band structure. The folded band undergoes a transition from positive to negative group velocity as the frequency is increased. At the transition frequency, the group velocity diverges and the average group refractive index vanishes, i.e., $n_g = \partial(n\omega)/\partial\omega = 0$ [35]. This point is known as the exceptional point (EP) associated with the coalescence of two modes and the opening of a “ k -gap” [36–40,43,44]. It should be noted that the folded bands in photonic systems [35,36,40] obtained previously are due to the assumption of nondispersive negative constitutive parameters, which is incompatible with causality, while the rotation-induced folded band here originates from a realistic model.

Since the zeros of the functions $\rho_e^-(\omega)$ and $B_e^{-1}(\omega)$ depend on the filling fraction f , the pattern of the entire band structure can vary drastically with a change of f . To investigate the variations in band structure induced by changing the filling fraction, it is convenient to consider the frequencies of the four band-edge states at the Brillouin zone boundaries [marked by ω_1 , ω_2 , ω_3 , and ω_4 in Fig. 1(b)], which can be obtained explicitly from Eqs. (9) and (6). At $k = 0$, ω_1 and ω_2 are

determined by the conditions of $\rho_e^-(\omega_1) = 0$ and $B_e^{-1}(\omega_2) = 0$. For ω_3 and ω_4 , for convenience, we take $k = \infty$ in Eq. (9) and look for the conditions of $\rho_e^+(\omega_3) + \rho_e^-(\omega_3) = 0$ and $B_e^{-1}(\omega_4) = \infty$, respectively. The analytical solutions of ω_1 , ω_2 , ω_3 , and ω_4 are

$$\begin{aligned} \omega_1 &= \frac{(1+f)\rho_s\Omega}{(1+f)\rho_s + (1-f)\rho_0}, \\ \omega_2 &= \sqrt{\frac{(1-f)\rho_s c_s^2 - 2f\rho_0 c_0^2}{f\rho_0 c_0^2 + (1-f)\rho_s c_s^2}}, \\ \omega_3 &= \sqrt{\frac{(1-f^2)\rho_s^2}{(1-f^2)(\rho_0^2 + \rho_s^2) + 2(1+f^2)\rho_0\rho_s}} \Omega, \\ \omega_4 &= \Omega \end{aligned} \quad (10)$$

and their dependence on f is shown in Fig. 2(a). We note that $\omega_4 = \Omega$ is independent of f . It is interesting to see that ω_2 , as a rapidly decreasing function of f , intersects with ω_1 and ω_3 . The dramatic change of band dispersions occurs near the filling fractions at which two band edges merge. When ω_2 intersects ω_1 at $f \approx 0.2111$, the folded band shrinks to a point [Fig. 2(b)]. The folded band reemerges as f is further increased, but is inverted with ω_2 lying below ω_1 [Fig. 2(c)]. When f approaches 0.2554, $\omega_2 \approx \omega_3$ with the two lowest bands almost touching [Fig. 2(d)]. When f is above 0.2554, ω_2 lies below ω_3 and the first band becomes folded [Fig. 2(e)]. Finally, ω_2 approaches zero when $f \approx 1/3$, above which the first band disappears and the system becomes gapped with a cutoff frequency at ω_3 [Fig. 2(f)]. The presence of a zero-frequency gap has its origin in the negativity of B_e^{-1} at low frequencies when f is sufficiently large. In fact, it can be shown that a single spinning cylinder has a negative response to an external applied force at a low frequency due to the antiresonant nature of B_{es}^{-1} shown in Eq. (6) (detailed analysis can be found in Appendix C).

III. DISPERSION RELATION AND ROBUST PROPAGATION OF INTERFACE STATES

In a 2D system, the acoustic wave equation has the same form as the electromagnetic wave equation (for one specific polarization), and the acoustic and electromagnetic parameters have a one-to-one mapping, $1/B \leftrightarrow \epsilon$, $\rho \leftrightarrow \mu$, when the electric field is parallel to the cylinder axis. In the presence of rotation, according to Eq. (7) our model is similar to a gyromagnetic photonic crystal under an external dc magnetic field, which induces the imaginary off-diagonal terms in μ [45,46]. As such, the spinning of cylinders plays the counterpart of an effective static magnetic field, which breaks the time-reversal symmetry and reciprocity, mimicking a quantum Hall system under an external magnetic field. If we combine the lattice with anticlockwise spinning cylinders and that with clockwise spinning cylinders (mimicking the magnetic field applied antiparallel to the gyromagnetic photonic crystal), we would expect the interface states to exist in the subwavelength band gap. However, there is one important difference. While the presence of the magnetic field changes μ without affecting the electric permittivity ϵ , the rotation of cylinders in our system

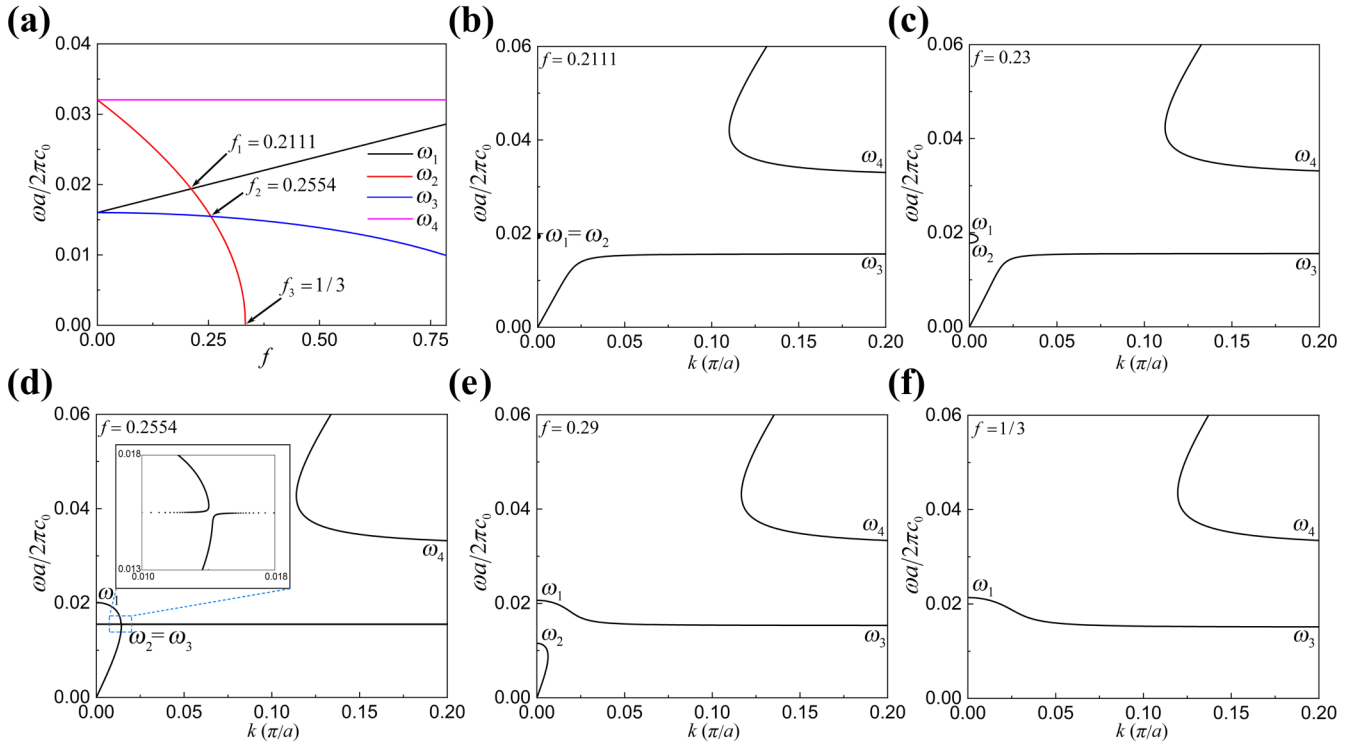


FIG. 2. (a) Frequencies of four band-edge states vs filling fraction f . (b)–(f) Evolution of bulk bands with increasing f . When $f > 1/3$, ω_3 becomes a cutoff frequency below which acoustic waves cannot propagate.

not only produces an antiresonance in B_e^{-1} , but also breaks the chiral symmetry of effective-mass densities. As we will show below, this antiresonance can also fold an interface-state band so that the interface states within the same band can propagate in two opposite directions in two different portions of an interface band.

We now investigate the dispersion relation of interface states. We consider two semi-infinite media separated by a boundary at $y = 0$, each having spinning cylinders at the same filling fraction but whose angular velocities display different signs (Ω for $y < 0$ and $-\Omega$ for $y > 0$). The pressure of the interface states takes the form $p = p_0 e^{ik_x x - \beta|y| - i\omega t}$, and by applying EMT, the dispersion relation and propagation constant can be solved as

$$k_x^2 = \frac{(\rho_e^+ + \rho_e^-)\omega^2}{2B_e} \quad \text{with} \quad \beta = -\frac{\rho_e^+ - \rho_e^-}{\rho_e^+ + \rho_e^-} k_x > 0. \quad (11)$$

Since β is positive in Eq. (11), these interface states are unidirectional. The sign of k_x is determined by the relative magnitudes of ρ_e^+ and ρ_e^- and it can therefore have different signs in different bands. Moreover, an additional nondispersive flat band occurs at frequency ω_1 where $\rho_e^- = 0$, i.e.,

$$\rho_e^- = 0 \quad \text{with} \quad \beta = k_x > 0. \quad (12)$$

This flat band has zero group velocity and does not transport energy. Similar flat bands were found previously at the interface of two magnetic domains in a Hermitian system [47]. The detailed derivations of the dispersion relations of interface states and the flat band can be found in Appendix D.

We now use MST to numerically verify the interface state dispersion derived above. We construct a supercell with 10 cylinders rotating anticlockwise in the region $y < 0$ and 10

cylinders rotating clockwise in the region $y > 0$. The periodic boundary condition is applied on the two edges of the supercell. For the case of $f = 0.15$, the four lowest interface-state bands calculated by MST are shown by the blue circles in Fig. 3(a). Also plotted in Fig. 3(a) is the result of EMT given in Eqs. (11) and (12) (red solid lines) with the effective parameters shown in Fig. 3(b). Again, excellent agreement is found. Unlike the projected bulk bands (green shaded region), where the dispersions are symmetric for the positive and negative k solutions, interface bands appear only on one side of k_x determined by the condition of $\beta > 0$ according to Eqs. (11) and (12). Thus, the sign of k_x can vary from band to band as shown in Fig. 3(a). For the three dispersive interface bands, only a portion of the second band lies within the absolute gap of the projected bulk bands. The lowest and the third interface bands overlap spectrally with the corresponding bulk bands. Similar to the case of the folded bulk band, we find also a transition point at which the group velocity diverges and the average group refractive index for the interface states vanishes, i.e., $n_g^{(s)} = 0$ [35]. The third band is also folded, and this band lies very close to the bulk band due to the fact that $\rho_e^+ - \rho_e^- \rightarrow 0$ at high frequencies, as clearly depicted in Fig. 3(b). As a result, the decay length diverges and the dispersion relations of the interface states and bulk states merge, as shown in Eqs. (11) and (9).

To explicitly demonstrate the interface states, we show in Figs. 3(c) and 3(d) the amplitude of the pressure field of the two eigenstates calculated by MST: one is in the first band and the other is in the second band. Both states exhibit an exponential decay behavior away from the interface. To determine the decay coefficient β , in Figs. 3(e) and 3(f) we plot the magnitude of the average field inside the cylinders

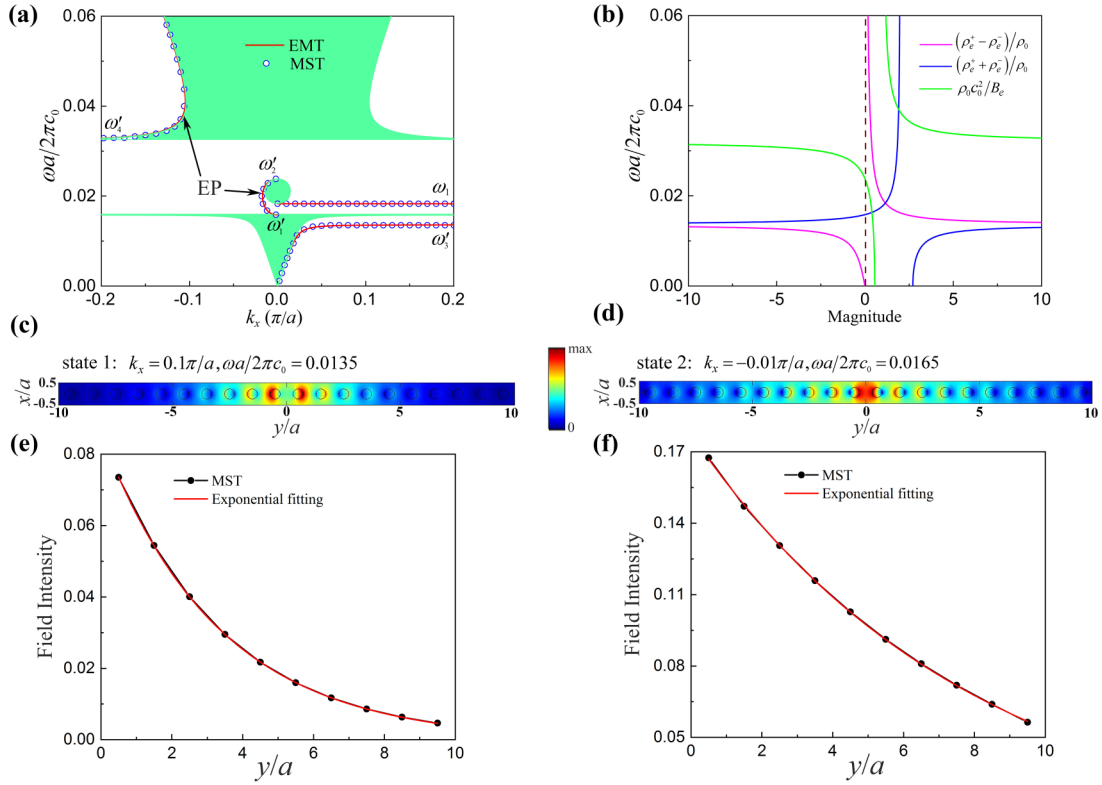


FIG. 3. (a) Interface state dispersion relations calculated by MST and EMT at $f = 0.15$. ω_1 is the frequency of the flat band. ω'_1 , ω'_2 , ω'_3 , and ω'_4 denote the frequencies at the Brillouin zone center and boundaries. The green shaded regions represent the projected bulk bands along the x direction. (b) Effective-mass densities and compressibility. Parts (c) and (d) are the absolute values of the pressure field distribution of two eigenstates in the first and second interface-state bands, respectively. Parts (e) and (f) are the intensities of the average field inside all cylinders on the $y > 0$ side for the two states in (c) and (d), respectively. The MST calculated field intensities can be well fitted using exponential functions decaying away from the boundaries at $y = 0$. For (e) and (f), the fitted exponential functions are $f(y) = 0.0741 \exp(-3.026y) - 0.00027$ and $f(y) = 0.1611 \exp(-1.232y) - 0.0044$, respectively.

on one side of the supercell as a function of the distance away from the interface. The results of exponential fittings give the values of β of these two states as 3.026 and 1.232, respectively, which agree well with the values of 3.021 and 1.217 obtained from Eq. (10).

In addition, we choose an interface state in the flat band and plot the real and imaginary parts of the pressure field in Fig. 4(a). It clearly reveals that the average pressure in a supercell is approximately equal to zero, i.e., $p \approx 0$, which is consistent with the analytical derivation in Appendix D. For comparison, the real and imaginary parts of the pressure of another interface state belonging to a folded band are plotted in Fig. 4(b). It is found that $p \neq 0$.

Using the EMT result of Eqs. (11) and (6), we can analytically solve the frequencies of interface states on the Brillouin zone boundaries, marked by ω'_1 , ω'_2 , ω'_3 , and ω'_4 in Fig. 3(a),

$$\begin{aligned} \omega'_1 = \omega_3 &= \sqrt{\frac{(1-f^2)\rho_s^2}{(1-f^2)(\rho_0^2 + \rho_s^2) + 2(1+f^2)\rho_0\rho_s}} \Omega, \\ \omega'_2 = \omega_2 &= \sqrt{\frac{(1-f)\rho_s c_s^2 - 2f\rho_0 c_0^2}{f\rho_0 c_0^2 + (1-f)\rho_s c_s^2}} \Omega, \\ \omega'_3 &= \frac{(1-f)\rho_s}{(1-f)\rho_s + (1+f)\rho_0} \Omega, \quad \omega'_4 = \Omega. \end{aligned} \quad (13)$$

Except for ω'_4 , all other frequencies are also functions of the filling fraction f , which is again an important parameter that determines the pattern of interface-state bands. The evolution of interface states is demonstrated in Fig. 5. The curves of ω'_1 , ω'_2 , ω'_3 , and ω'_4 versus f are plotted in Fig. 5(a). Similar to the bulk band, ω'_2 has intersection points with ω'_1 and ω'_3 . The dispersion curves of interface states at different filling fractions are plotted in Figs. 5(b)–5(f). Also plotted are bulk bands for comparison. When $f = 0.2554$, $\omega'_1 = \omega'_2$, the second folded band almost shrinks to a point. As the filling fraction increases to $f = 0.28$, the folded band appears again but flips to the $k_x > 0$ region, which is due to the sign change of $\rho_e^+ + \rho_e^-$. When $f = 0.2915$, $\omega'_2 \approx \omega'_3$, the first and second bands nearly touch each other and behave as if they might merge together to form one band. When f continuously increases to 0.31, $\omega'_2 < \omega'_3$, the folded band descends to be the lowest band and it almost overlaps to the bulk band. When $f > 1/3$, the folded interface state band disappears with the folded bulk band. To the best of our knowledge, this unusual dispersion of interface states and their sensitive dependence on the filling fraction are not found in Hermitian systems.

To demonstrate the robustness of the one-way transport of the interface states, we choose the filling fraction $f = 0.2111$ as an example. The corresponding projected bulk bands and the interface states are shown in Fig. 6(a). In this case, since

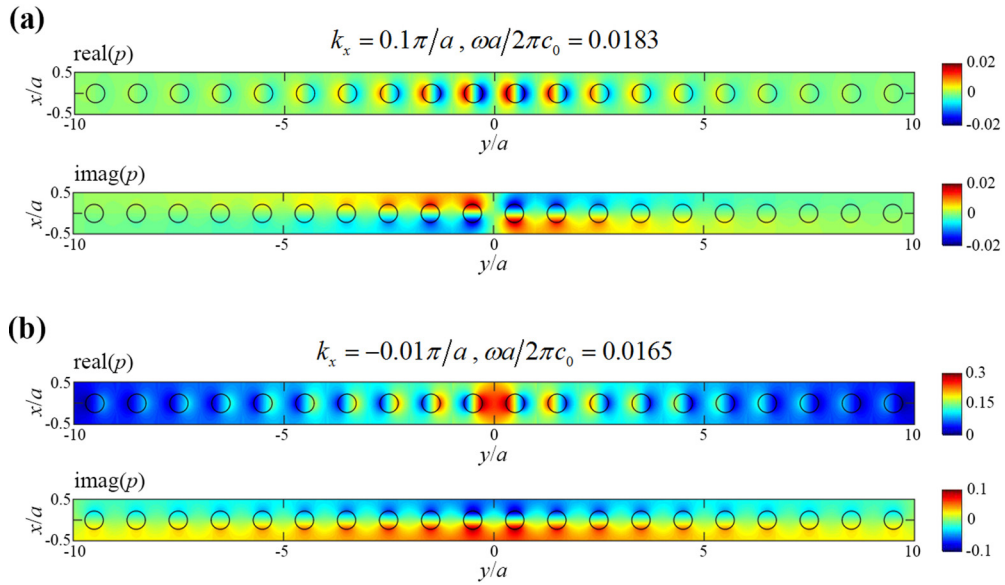


FIG. 4. The real and imaginary parts of an interface state that belongs to (a) a flat band and (b) a folded band, respectively.

the second folded bulk band shrinks almost to a point, a wider gap exists in the bulk band structure, making it easier to observe the robust one-way transport of interface states. Unlike the conventional topological interface-state bands, which typically have either a positive or a negative group velocity [14–19] within one band, our folded interface band possesses both positive and negative group velocities. The unidirectional

transmission of interface states along two different directions can be achieved at different frequencies in the same band. A finite-sized system that has a boundary with rectangular U-turns is purposely designed, as shown in the inset of Fig. 6(b). The cylinders above the interface rotate clockwise while those below the interface rotate anticlockwise, and the entire system is embedded in a static water background. A small amount

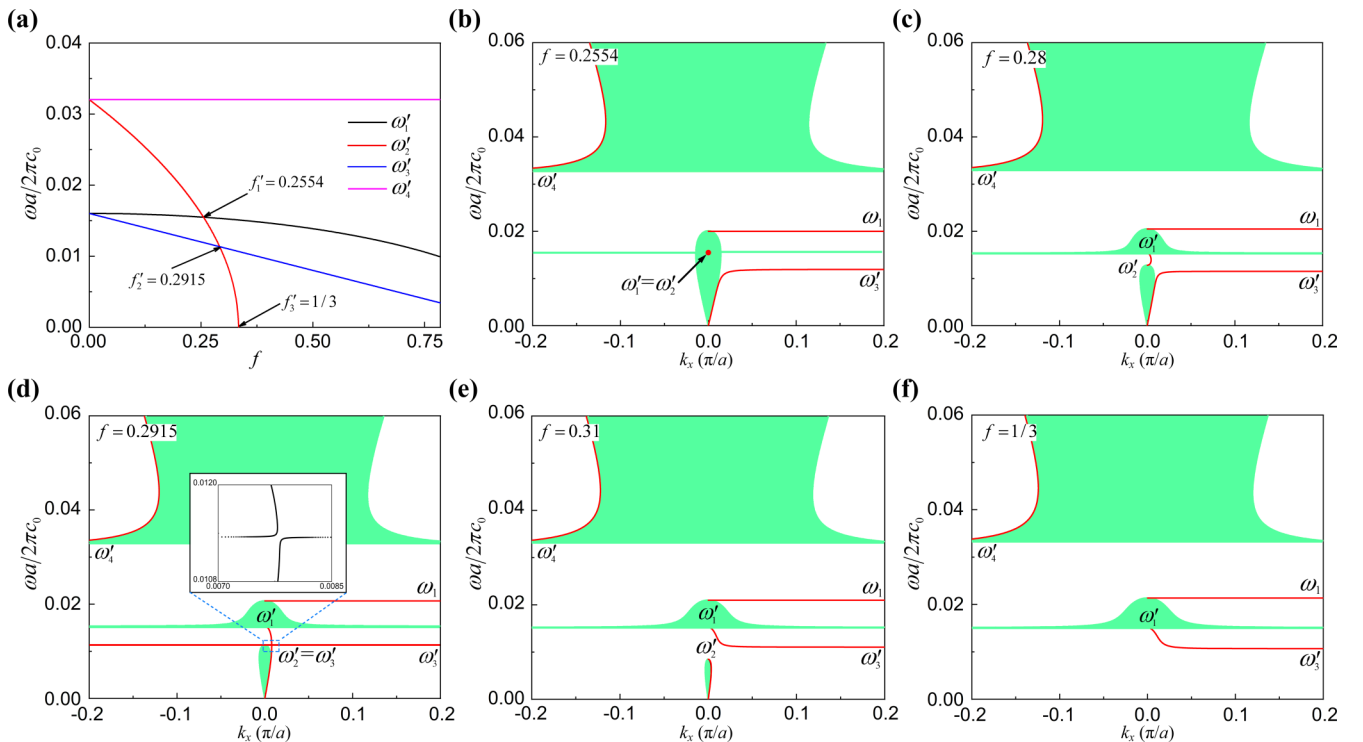


FIG. 5. (a) Frequencies of band edges as a function of the filling fraction. (b)–(f) The evolution of interface states (solid red lines) as the increase of the filling fraction. The green shaded regions represent the projected bulk bands along the x direction. When $f > 1/3$, the dispersion relation is similar to that of (f), in which a band gap appears below a cutoff frequency, showing that the rotating inclusions stop the propagation of low-frequency longitudinal waves in the bulk of the composite material.

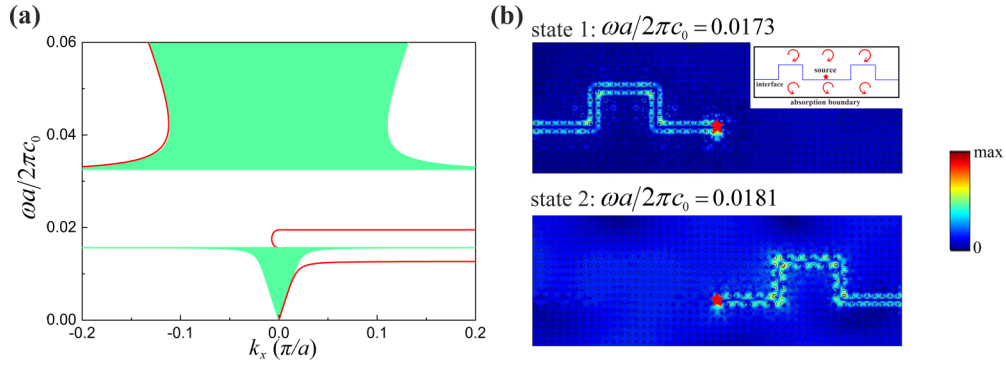


FIG. 6. (a) The projected bulk band (green shaded region) and interface states (red solid line) at a filling fraction $f = 0.2111$. (b) The wave with frequency $\omega a / 2\pi c_0 = 0.0173$ and that with $\omega a / 2\pi c_0 = 0.0181$ propagating along a convex-shaped interface in a finite system. The inset is the configuration of the structure. The blue line denotes the interface. The red arrows indicate the directions in which the cylinders rotate. The red stars mark the positions of point sources.

of absorption is added on the surrounding layer to prevent the reflection of acoustic waves at the sample-background boundary. A 2D point source is placed at the center of the structure [marked by the red star in Fig. 6(b)]. The frequency of the transition point in the folded interface-state band that marks the change from a positive to a negative group velocity is $\omega a / 2\pi c_0 = 0.0176$. Figure 6(b) clearly demonstrates that the excited interface wave propagates along the left side at frequency $\omega a / 2\pi c_0 = 0.0173$ and along the right side at frequency $\omega a / 2\pi c_0 = 0.0181$, without backscattering from the sharp corners. The directions of propagation are consistent with the signs of the group velocity shown in Fig. 6(a).

IV. CONCLUSION AND DISCUSSIONS

In this work, we investigate the dispersion relations of bulk band and interface states for an AM comprising spinning cylindrical fluidic inclusions embedded in a static fluid medium. Due to the antiresonance of effective compressibility and the rotational Doppler effect, which breaks the chiral symmetry of the effective-mass densities, folded bulk bands and interface-state bands are formed. By varying the filling ratio of the spinning cylinders, we found interesting evolutions of band structures for both bulk bands and interface-state bands. Remarkably, when the filling ratio exceeds some critical value, a zero-frequency gap appears. In addition, since the interface state band is folded, both positive and negative group velocities of acoustic waves can coexist in the same band. We have also numerically demonstrated the robust one-way propagation of interface waves with different directions in the same band.

In the present study, we have considered cylindrical inclusions that are fluidic. It would be interesting to consider rotating solid inclusions, in either fluidic or solid background media. Shear waves should be considered in those systems, and the multiple scattering formulation will get more challenging. As the interesting effects (including a rotation-induced low-frequency cutoff for high filling ratios, and antiresonance behavior in the effective compressibility) can be described by effective-medium theories, we expect that these novel phenomena do not depend on the symmetry of the lattice and should persist in a random or aperiodic array. Nevertheless,

the effect of disorder is an interesting direction to explore. Also, our analytic results show that the interesting effects do not require a critical minimum speed, meaning that if the rotational speed is reduced, the phenomena will not disappear but the band gaps will be smaller and the effects will become less conspicuous.

ACKNOWLEDGMENTS

This work was supported by the Hong Kong Research Grants Council under Grant No. AoE/P-02/12 and 16303119. D.Z. was also supported by the National Natural Science Foundation of China under Grant No. 11874168.

APPENDIX A: EFFECTIVE-MEDIUM PARAMETERS

Here, we derive the effective acoustic wave constitutive parameters for acoustic metamaterial with spinning cylinders. The required approximations of Bessel and Neumann functions as the argument tends to zero are listed in Table I. We begin from Eq. (4) in the main text, in which the Mie scattering coefficients are given by

$$D_m = -\frac{\lambda_m \rho_0 R_m(\lambda_m r_s) J_m(k_0 r_s) - k_0 \rho_s J_m(\lambda_m r_s) J'_m(k_0 r_s)}{\lambda_m \rho_0 R_m(\lambda_m r_s) H_m(k_0 r_s) - k_0 \rho_s J_m(\lambda_m r_s) H'_m(k_0 r_s)},$$

where

$$R_m(\lambda_m r_s) = \frac{\omega^2}{(4\Omega^2 + M^2)(\Omega^2 + M^2)} \left[(2\Omega^2 - M^2) J'_m(\lambda_m r_s) - 3imM\Omega \frac{J_m(\lambda_m r_s)}{\lambda_m r_s} \right].$$

Here $\lambda_m^2 = -(4\Omega^2 + M^2)c_s^{-2}$ and $M = -i(\omega - m\Omega)$. To calculate the effective density and bulk modulus, the following

TABLE I. Approximations of the Bessel and Neumann functions as $x \approx 0$.

$J_0(x) \approx 1$	$J_{\pm 1}(x) \approx \pm \frac{x}{2}$	$J'_0(x) \approx -\frac{x}{2}$	$J'_{\pm 1}(x) \approx \pm \frac{1}{2}$
$Y_0(x) \approx \frac{2}{\pi} \ln x$	$Y_{\pm 1}(x) \approx \mp \frac{2}{\pi x}$	$Y'_0(x) \approx \frac{2}{\pi x}$	$Y'_{\pm 1}(x) \approx \pm \frac{2}{\pi x^2}$

term $D_m/(1 + D_m)$ is needed [33]:

$$\begin{aligned} & \frac{D_m}{1 + D_m} \\ &= \frac{-\frac{\lambda_m \rho_0 R_m(\lambda_m r_s) J_m(k_0 r_s) - k_0 \rho_s J_m(\lambda_m r_s) J'_m(k_0 r_s)}{\lambda_m \rho_0 R_m(\lambda_m r_s) H_m(k_0 r_s) - k_0 \rho_s J_m(\lambda_m r_s) H'_m(k_0 r_s)}}{1 - \frac{\lambda_m \rho_0 R_m(\lambda_m r_s) J_m(k_0 r_s) - k_0 \rho_s J_m(\lambda_m r_s) J'_m(k_0 r_s)}{\lambda_m \rho_0 R_m(\lambda_m r_s) H_m(k_0 r_s) - k_0 \rho_s J_m(\lambda_m r_s) H'_m(k_0 r_s)}} \\ &= \frac{-\lambda_m \rho_0 R_m(\lambda_m r_s) J_m(k_0 r_s) + k_0 \rho_s J_m(\lambda_m r_s) J'_m(k_0 r_s)}{i \lambda_m \rho_0 R_m(\lambda_m r_s) Y_m(k_0 r_s) - i k_0 \rho_s J_m(\lambda_m r_s) Y'_m(k_0 r_s)}. \end{aligned} \quad (\text{A1})$$

Based on the multiple scattering theory, under the standard approximations $k_0 r_0, k_0 r_s \ll 1$, the effective bulk modulus B_e , which is determined by $m = 0$ terms, can be denoted as

$$\frac{B_e^{-1} + 2B_0^{-1} \frac{J'_0(k_0 r_0)}{k_0 r_0 J_0(k_0 r_0)}}{B_e^{-1} + 2B_0^{-1} \frac{Y'_0(k_0 r_0)}{k_0 r_0 Y_0(k_0 r_0)}} = \frac{Y_0(k_0 r_0)}{i J_0(k_0 r_0)} \left(\frac{D_0}{1 + D_0} \right). \quad (\text{A2})$$

The right-hand side (RHS) of Eq. (A2) is

RHS

$$\begin{aligned} &= \frac{Y_0(k_0 r_0) \lambda_0 \rho_0 R_0(\lambda_0 r_s) J_0(k_0 r_s) - k_0 \rho_s J_0(\lambda_0 r_s) J'_0(k_0 r_s)}{J_0(k_0 r_0) \lambda_0 \rho_0 R_0(\lambda_0 r_s) Y_0(k_0 r_s) - k_0 \rho_s J_0(\lambda_0 r_s) Y'_0(k_0 r_s)} \\ &\approx \frac{2}{\pi} \ln k_0 r_0 \frac{\lambda_0 \rho_0 R_0(\lambda_0 r_s) + k_0 \rho_s J_0(\lambda_0 r_s) \frac{k_0 r_s}{2}}{\lambda_0 \rho_0 R_0(\lambda_0 r_s) \frac{2}{\pi} \ln k_0 r_s - k_0 \rho_s J_0(\lambda_0 r_s) \frac{2}{\pi k_0 r_s}} \\ &= \frac{2}{\pi} \ln k_0 r_0 \frac{\lambda_0 \rho_0 R_0(\lambda_0 r_s) + k_0 \rho_s J_0(\lambda_0 r_s) \frac{k_0 r_s}{2}}{\ln k_0 r_s \left[\lambda_0 \rho_0 R_0(\lambda_0 r_s) \frac{2}{\pi} - k_0 \rho_s J_0(\lambda_0 r_s) \frac{2}{\pi k_0 r_s \ln k_0 r_s} \right]} \\ &\approx \frac{2}{\pi} \ln k_0 r_0 \frac{\lambda_0 \rho_0 R_0(\lambda_0 r_s) + k_0 \rho_s J_0(\lambda_0 r_s) \frac{k_0 r_s}{2}}{-k_0 \rho_s J_0(\lambda_0 r_s) \frac{2}{\pi k_0 r_s}} \\ &= \frac{-\frac{2\lambda_0 \rho_0 R_0(\lambda_0 r_s)}{k_0 \rho_s J_0(\lambda_0 r_s) k_0 r_s} - 1}{\frac{2}{k_0^2 r_s^2 \ln k_0 r_0}}. \end{aligned} \quad (\text{A3})$$

The left-hand side (LHS) of Eq. (A2) is

$$\begin{aligned} \text{LHS} &= \frac{B_e^{-1} + 2B_0^{-1} \frac{J'_0(k_0 r_0)}{k_0 r_0 J_0(k_0 r_0)}}{B_e^{-1} + 2B_0^{-1} \frac{Y'_0(k_0 r_0)}{k_0 r_0 Y_0(k_0 r_0)}} \approx \frac{B_e^{-1} - B_0^{-1}}{B_e^{-1} + 2B_0^{-1} \frac{\frac{2}{\pi k_0 r_0}}{k_0 r_0 \frac{2}{\pi} \ln k_0 r_0}} \\ &= \frac{B_e^{-1} - B_0^{-1}}{B_e^{-1} + 2B_0^{-1} \frac{1}{k_0^2 r_0^2 \ln k_0 r_0}} \approx \frac{B_e^{-1} - B_0^{-1}}{B_0^{-1} \frac{2}{k_0^2 r_0^2 \ln k_0 r_0}}. \end{aligned} \quad (\text{A4})$$

Compare Eqs. (A3) and (A4),

$$\frac{B_e^{-1} - B_0^{-1}}{B_0^{-1}} = \left(\frac{r_s}{r_0} \right)^2 \frac{B_{es}^{-1} - B_0^{-1}}{B_0^{-1}} = f \frac{B_{es}^{-1} - B_0^{-1}}{B_0^{-1}}, \quad (\text{A5})$$

where $f = (r_s/r_0)^2$ represents the filling fraction of the crystal, and B_{es} can be regarded as the bulk modulus of a spinning cylinder seen in the lab frame and can be approximated as

$$\begin{aligned} B_{es}^{-1} &= -\frac{2\lambda_0 R_0(\lambda_0 r_s)}{k_0 \rho_s c_s^2 J_0(\lambda_0 r_s) k_0 r_s} \\ &= -\frac{2\lambda_0 R_0(\lambda_0 r_s)}{\omega^2 \rho_s r_s J_0(\lambda_0 r_s)} \end{aligned}$$

$$\begin{aligned} &= -\frac{2\lambda_0}{\omega^2 \rho_s r_s J_0(\lambda_0 r_s)} \frac{\omega^2}{(4\Omega^2 + M^2)(\Omega^2 + M^2)} \\ &\quad \times [(2\Omega^2 - M^2) J'_0(\lambda_0 r_s)] \\ &\approx \frac{\lambda_0^2}{\rho_s} \frac{(2\Omega^2 - M^2)}{(4\Omega^2 + M^2)(\Omega^2 + M^2)} \\ &= -\frac{2\Omega^2 - M^2}{\rho_s c_s^2 (\Omega^2 + M^2)} \\ &= \frac{2\Omega^2 + \omega^2}{\rho_s c_s^2 (\omega^2 - \Omega^2)}. \end{aligned} \quad (\text{A6})$$

Then

$$B_e^{-1} = f B_{es}^{-1} + (1 - f) B_0^{-1} = \frac{f}{\rho_s c_s^2} \frac{2\Omega^2 + \omega^2}{\omega^2 - \Omega^2} + \frac{1 - f}{\rho_0 c_0^2}. \quad (\text{A7})$$

For effective-mass density, we first take the angular index $m = 1$ into account. The effective-mass density ρ_e^+ can be denoted as [33]

$$\frac{\rho_e^+ - \rho_0 \frac{J_1(k_0 r_0)}{k_0 r_0 J'_1(k_0 r_0)}}{\rho_e^+ - \rho_0 \frac{Y_1(k_0 r_0)}{k_0 r_0 Y'_1(k_0 r_0)}} = \frac{Y'_1(k_0 r_0)}{i J'_1(k_0 r_0)} \left(\frac{D_1}{1 + D_1} \right). \quad (\text{A8})$$

The RHS of Eq. (A8) can be approximated as

RHS

$$\begin{aligned} &= \frac{Y'_1(k_0 r_0) \lambda_1 \rho_0 R_1(\lambda_1 r_s) J_1(k_0 r_s) - k_0 \rho_s J_1(\lambda_1 r_s) J'_1(k_0 r_s)}{J'_1(k_0 r_0) \lambda_1 \rho_0 R_1(\lambda_1 r_s) Y_1(k_0 r_s) - k_0 \rho_s J_1(\lambda_1 r_s) Y'_1(k_0 r_s)} \\ &\approx \frac{4}{\pi k_0^2 r_0^2} \frac{\lambda_1 \rho_0 R_1(\lambda_1 r_s) \frac{k_0 r_s}{2} - k_0 \rho_s J_1(\lambda_1 r_s) \frac{1}{2}}{\lambda_1 \rho_0 R_1(\lambda_1 r_s) \left(-\frac{2}{\pi k_0 r_s} \right) - k_0 \rho_s J_1(\lambda_1 r_s) \frac{2}{\pi k_0^2 r_s^2}} \\ &= \frac{r_s^2}{r_0^2} \frac{\lambda_1 \rho_0 R_1(\lambda_1 r_s) r_s - \rho_s J_1(\lambda_1 r_s)}{-\lambda_1 \rho_0 R_1(\lambda_1 r_s) r_s - \rho_s J_1(\lambda_1 r_s)} \\ &= f \frac{\rho_s \frac{J_1(\lambda_1 r_s)}{\lambda_1 r_s R_1(\lambda_1 r_s)} - \rho_0}{\rho_s \frac{J_1(\lambda_1 r_s)}{\lambda_1 r_s R_1(\lambda_1 r_s)} + \rho_0}. \end{aligned} \quad (\text{A9})$$

The LHS of Eq. (A8) is expressed as

$$\text{LHS} = \frac{\rho_e^+ - \rho_0 \frac{J_1(k_0 r_0)}{k_0 r_0 J'_1(k_0 r_0)}}{\rho_e^+ - \rho_0 \frac{Y_1(k_0 r_0)}{k_0 r_0 Y'_1(k_0 r_0)}} \approx \frac{\rho_e^+ - \rho_0}{\rho_e^+ + \rho_0}. \quad (\text{A10})$$

Combining Eqs. (A9) and (A10), we have

$$\frac{\rho_e^+ - \rho_0}{\rho_e^+ + \rho_0} = f \frac{\rho_{es}^+ - \rho_0}{\rho_{es}^+ + \rho_0}, \quad (\text{A11})$$

which can be reexpressed as

$$\rho_e^+ = \rho_0 \frac{(1 + f) \rho_{es}^+ + (1 - f) \rho_0}{(1 - f) \rho_{es}^+ + (1 + f) \rho_0}, \quad (\text{A12})$$

where ρ_{es}^+ represents the effective-mass density of a spinning cylinder seen in the lab frame and has the form

$$\begin{aligned}
\rho_{es}^+ &= \rho_s \frac{J_1(\lambda_1 r_s)}{\lambda_1 r_s R_1(\lambda_1 r_s)} \\
&= \rho_s \frac{J_1(\lambda_1 r_s)}{\lambda_1 r_s \frac{\omega^2}{(4\Omega^2 + M^2)(\Omega^2 + M^2)} [(2\Omega^2 - M^2)J_1'(\lambda_1 r_s) - 3iM\Omega \frac{J_1(\lambda_1 r_s)}{\lambda_1 r_s}]} \\
&= \rho_s \frac{(4\Omega^2 + M^2)(\Omega^2 + M^2)}{\omega^2 [(2\Omega^2 - M^2)\lambda_1 r_s \frac{J_1'(\lambda_1 r_s)}{J_1(\lambda_1 r_s)} - 3iM\Omega]} \\
&= \rho_s \frac{[4\Omega^2 - (\omega - \Omega)^2][\Omega^2 - (\omega - \Omega)^2]}{\omega^2 [2\Omega^2 + (\omega - \Omega)^2] - 3(\omega - \Omega)\Omega} \\
&= \rho_s \frac{(3\Omega^2 - \omega^2 + 2\omega\Omega)(-\omega^2 + 2\omega\Omega)}{\omega^2(\omega^2 + 6\Omega^2 - 5\omega\Omega)} \\
&= \rho_s \frac{(\omega - 3\Omega)(\omega + \Omega)\omega(\omega - 2\Omega)}{\omega^2(\omega - 2\Omega)(\omega - 3\Omega)} \\
&= \rho_s \left(1 + \frac{\Omega}{\omega}\right). \tag{A13}
\end{aligned}$$

Similarly, for $m = -1$ we can get

$$\rho_e^- = \rho_0 \frac{(1+f)\rho_{es}^- + (1-f)\rho_0}{(1-f)\rho_{es}^- + (1+f)\rho_0} \quad \text{with} \quad \rho_{es}^- = \rho_s \left(1 - \frac{\Omega}{\omega}\right). \tag{A14}$$

APPENDIX B: DERIVATION OF MASS DENSITY TENSOR IN CARTESIAN COORDINATES

Euler's equation of acoustic wave is

$$\rho \frac{\partial \vec{v}}{\partial t} = \vec{F} = -\nabla p. \tag{B1}$$

Here the vector \vec{F} denotes the force per unit volume. For a two-dimensional system, in Cartesian coordinates, the equation can be expressed as

$$-i\omega \begin{pmatrix} \rho_{xx} & \rho_{xy} \\ \rho_{yx} & \rho_{yy} \end{pmatrix} \begin{pmatrix} v_x \\ v_y \end{pmatrix} = \begin{pmatrix} F_x \\ F_y \end{pmatrix}. \tag{B2}$$

In the case of $m = \pm 1$, the above equation can be expressed as

$$-i\omega \begin{pmatrix} \rho_e^+ & 0 \\ 0 & \rho_e^- \end{pmatrix} \begin{pmatrix} v^+ \\ v^- \end{pmatrix} = \begin{pmatrix} F^+ \\ F^- \end{pmatrix}. \tag{B3}$$

The transformation between $m = \pm 1$ unit vectors and those in Cartesian coordinates is

$$\begin{aligned}
e^+ &= \frac{1}{\sqrt{2}}(\hat{x} + i\hat{y}), \\
e^- &= \frac{1}{\sqrt{2}}(\hat{x} - i\hat{y}).
\end{aligned} \tag{B4}$$

Then

$$\begin{aligned}
\vec{F} &= F^+ \hat{e}^+ + F^- \hat{e}^- = F^+ \frac{1}{\sqrt{2}}(\hat{x} + i\hat{y}) + F^- \frac{1}{\sqrt{2}}(\hat{x} - i\hat{y}) \\
&= F_x \hat{x} + F_y \hat{y},
\end{aligned} \tag{B5}$$

where $F^\pm = (1/\sqrt{2})(F_x \mp iF_y)$. The transformation of components between a two-coordinate system can be written as

$$\begin{pmatrix} F_x \\ F_y \end{pmatrix} = \frac{1}{\sqrt{2}} \begin{pmatrix} 1 & 1 \\ i & -i \end{pmatrix} \begin{pmatrix} F^+ \\ F^- \end{pmatrix} = U \begin{pmatrix} F^+ \\ F^- \end{pmatrix}. \tag{B6}$$

Similarly, we have

$$\begin{pmatrix} v_x \\ v_y \end{pmatrix} = U \begin{pmatrix} v^+ \\ v^- \end{pmatrix}. \tag{B7}$$

Combining Eqs. (B2), (B3), (B6), and (B7), the mass density tensor in Cartesian coordinates can be obtained as

$$\begin{aligned}
\begin{pmatrix} \rho_{xx} & \rho_{xy} \\ \rho_{yx} & \rho_{yy} \end{pmatrix} &= U \begin{pmatrix} \rho_e^+ & 0 \\ 0 & \rho_e^- \end{pmatrix} U^{-1} \\
&= \frac{1}{2} \begin{pmatrix} \rho_e^+ + \rho_e^- & -i(\rho_e^+ - \rho_e^-) \\ i(\rho_e^+ - \rho_e^-) & \rho_e^+ + \rho_e^- \end{pmatrix}.
\end{aligned} \tag{B8}$$

In the limit of $f \rightarrow 1$, Eq. (A12) reduces to $\rho_e^\pm = \rho_{es}^\pm$. Equation (B3) can also be independently derived by the wave scattering of a single spinning cylinder. In polar coordinate, according to Eq. (B1) the components of \vec{F} are

$$F_r = -\frac{\partial p}{\partial r}, \quad F_\theta = -\frac{\partial p}{r \partial \theta} = -\frac{ip}{r}. \tag{B9}$$

According to Eq. (14) of [27], we have

$$\begin{aligned}
\rho_0(M^2 + 4\Omega^2)v_r &= MF_r + 2\Omega F_\theta, \\
\rho_0(M^2 + 4\Omega^2)v_\theta &= -2\Omega F_r + MF_\theta.
\end{aligned} \tag{B10}$$

In the case of $m = -1$, Eq. (B10) gives

$$\rho_0(M^2 + 4\Omega^2)(v_r + iv_\theta) = (M - 2i\Omega)(F_r + iF_\theta). \tag{B11}$$

Or,

$$\rho_0(-i\omega) \left(1 - \frac{\Omega}{\omega}\right) (v_r + iv_\theta) = F_r + iF_\theta. \tag{B12}$$

According to the transformation between polar and Cartesian coordinates, we have

$$F_r + iF_\theta = e^{-i\theta}(F_x + iF_y), \quad v_r + iv_\theta = e^{-i\theta}(v_x + iv_y). \quad (\text{B13})$$

Thus, Eq. (B12) can be written as

$$-i\omega\rho_{es}^-v^- = F^-. \quad (\text{B14})$$

Similarly, when $m = 1$, we use

$$\rho_0(M^2 + 4\Omega^2)(v_r - iv_\theta) = (M + 2i\Omega)(F_r - iF_\theta)$$

and

$$F_r - iF_\theta = e^{i\theta}(F_x - iF_y), \quad v_r - iv_\theta = e^{i\theta}(v_x - iv_y)$$

to obtain

$$-i\omega\rho_0\left(1 + \frac{\Omega}{\omega}\right)v^+ \equiv -i\omega\rho_{es}^+v^+ = F^+. \quad (\text{B15})$$

APPENDIX C: INDEPENDENT ANALYSIS ABOUT EFFECTIVE BULK MODULUS OF SINGLE SPINNING CYLINDER AND ZERO-FREQUENCY GAP WITH HIGH FILLING FRACTION

Here we consider the scattering of acoustic waves by one single spinning cylinder. In low frequencies, the effective bulk modulus is determined by the $m = 0$ component of the Mie scattering coefficient. Under this condition, according to Eq. (19) in [27], the radial displacement in a rotational cylinder denotes

$$u_r = \frac{2\Omega^2 + \omega^2}{(4\Omega^2 - \omega^2)(\Omega^2 - \omega^2)} \frac{\partial_r p}{\rho_s}. \quad (\text{C1})$$

The acoustic wave equation in a rotational cylinder is

$$\frac{1}{r} \frac{\partial}{\partial r} \left(r \frac{\partial p}{\partial r} \right) + \lambda_0^2 p = 0, \quad (\text{C2})$$

where $\lambda_0 = \sqrt{-(4\Omega^2 - \omega^2)c_s^{-2}}$ is the rotating wave number for $m = 0$. By solving Eq. (C2), under the low-frequency approximation, we have

$$p \approx A_0 J_0(\lambda_0 r) \approx A_0, \quad \partial_r p \approx -\frac{\lambda_0^2 r}{2} A_0 = \frac{4\Omega^2 - \omega^2}{2c_s^2} r A_0, \quad (\text{C3})$$

where A_0 is the amplitude of pressure in low frequencies, and here we set $A_0 > 0$ to denote a positive pressure. Substituting Eq. (C3) into Eq. (C1), we have

$$\frac{u_r}{r} = \frac{2\Omega^2 + \omega^2}{2\rho_s c_s^2 (\Omega^2 - \omega^2)} A_0. \quad (\text{C4})$$

Based on the definition of bulk modulus $B = -V(\partial p / \partial V)$, we have

$$\begin{aligned} B_{es} &\approx -V \frac{\Delta p}{\Delta V} = -\pi r^2 h \frac{p}{2\pi r u_r h} \approx -\frac{r}{2u_r} A_0 \\ \Rightarrow B_{es}^{-1} &\approx -\frac{2u_r}{r A_0} = \frac{1}{\rho_s c_s^2} \frac{2\Omega^2 + \omega^2}{\omega^2 - \Omega^2}. \end{aligned} \quad (\text{C5})$$

The result is identical to Eq. (A6) in Appendix A, which is derived by the effective-medium theory of [33]. In Eq. (C5), we have

$$\Delta V = 2\pi r u_r h = \frac{\pi r^2 h}{\rho_s c_s^2} \frac{2\Omega^2 + \omega^2}{\Omega^2 - \omega^2} A_0 \quad (\text{C6})$$

when frequency $\omega \rightarrow 0$, $\Delta V = 2\pi r^2 h A_0 / \rho_s c_s^2 > 0$. It means that under a positive pressure, the volume of a cylinder expands instead of compresses, i.e., the spinning cylinder exhibits a negative effective bulk modulus. And the effective bulk modulus of the whole system is the weighted mean of bulk modulus for cylinder and background,

$$B_e^{-1} = f B_{es}^{-1} + (1 - f) B_0^{-1}. \quad (\text{C7})$$

As f increases, the effect of expansion of the rotational cylinder increases, while that of compression of the static background decreases. When $f > 1/3$, the expansion becomes greater than compression, and the system has a negative response under the applied pressure. Then $B_e^{-1} < 0$ and the band gap appears.

APPENDIX D: DERIVATION OF DISPERSIVE AND NONDISPERSIVE BANDS OF INTERFACE STATES

Due to mirror symmetry, the pressure and velocity of the interface states take the form $p = p_0 e^{ik_x x - \beta|y| - i\omega t}$ and $\vec{v} = (v_x \hat{x} + v_y \hat{y}) = v_x 0 e^{ik_x x - \beta|y| - i\omega t} \hat{x} + v_y 0 e^{ik_x x - \beta|y| - i\omega t} \hat{y}$, respectively, with $\beta > 0$ denoting the decay coefficient [47]. Euler's equation can be written as $\vec{\rho}_e(\partial \vec{v} / \partial t) = -\nabla p$ in the region $y < 0$ and $\vec{\rho}_e^*(\partial \vec{v} / \partial t) = -\nabla p$ in region $y > 0$, where $\vec{\rho}_e^*$ is the complex conjugate of $\vec{\rho}_e$ in Eq. (7) in the main text due to the sign change of Ω . By using the boundary conditions that p and v_y are continuous at the interface $y = 0$, we obtain the relation

$$k_x = -\frac{\rho_e^+ + \rho_e^-}{\rho_e^+ - \rho_e^-} \beta. \quad (\text{D1})$$

Substituting Eq. (D1) into the dispersion relation Eq. (9) with k^2 replaced by $k_x^2 - \beta^2$ on the left-hand side, we obtain the following dispersion relation for the interface states:

$$k_x^2 = \frac{(\rho_e^+ + \rho_e^-)\omega^2}{2B_e}. \quad (\text{D2})$$

Under the condition $\rho_e^- = 0$, in the region $y < 0$, Euler's equation can be written as

$$\frac{i\omega\rho_e^+}{2} \begin{pmatrix} 1 & -i \\ i & 1 \end{pmatrix} \begin{pmatrix} v_x \\ v_y \end{pmatrix} = \begin{pmatrix} ik_x \\ \beta \end{pmatrix} p. \quad (\text{D3})$$

Equation (D3) has two sets of solutions: solution 1 is $k_x = -\beta$ with $p \neq 0$ and solution 2 is $p = 0$.

For solution 1, we apply condition $\rho_e^- = 0$ and solution $k_x = -\beta$ in a continuity equation of acoustic wave $B_e \nabla \cdot \vec{v} = -\partial p / \partial t$, and we have

$$B_e(ik_x v_x + \beta v_y) = B_e \beta (-iv_x + v_y) = i\omega p. \quad (\text{D4})$$

Combining Eqs. (D3) and (D4), we have the solutions

$$\begin{aligned} v_x &= \left(\frac{k_x}{\omega\rho_e^+} + \frac{\omega}{2B_e k_x} \right) p, \\ v_y &= \left(-\frac{\omega}{2B_e k_x} + \frac{k_x}{\omega\rho_e^+} \right) ip. \end{aligned} \quad (\text{D5})$$

Similarly, in the $y > 0$ region, we can obtain the solutions

$$\begin{aligned} v_x &= \left(\frac{k_x}{\omega\rho_e^+} + \frac{\omega}{2B_e k_x} \right) p, \\ v_y &= \left(-\frac{k_x}{\omega\rho_e^+} + \frac{\omega}{2B_e k_x} \right) ip. \end{aligned} \quad (\text{D6})$$

Applying the boundary condition $v_{y(y<0)} = v_{y(y>0)}$ at the interface, according to Eqs. (D5) and (D6), we have two solutions. One is $k_x^2 = \rho_e^+ \omega^2 / 2B_e$, which belongs to the dispersion relation of interface state Eq. (10) with $\rho_e^- = 0$. The other

solution is $p = 0$, which is inconsistent with the precondition $p \neq 0$. Then the first solution is only a point in the dispersive interface states band.

For the second solution, i.e., $p = 0$, in the $y < 0$ area, Euler's equation gives

$$v_x - iv_y = 0. \quad (\text{D7})$$

The continuity equation gives

$$B_e(ik_x v_x + \beta v_y) = 0. \quad (\text{D8})$$

Combining Eqs. (D7) and (D8), we have the solution

$$k_x = \beta, \quad (\text{D9})$$

i.e., the dispersion relation of a flat interface state band, and the same solution can be obtained in the $y > 0$ region.

-
- [1] S. Zhang, L. Yin, and N. Fang, *Phys. Rev. Lett.* **102**, 194301 (2009).
- [2] J. Li, L. Fok, X. Yin, G. Bartal, and X. Zhang, *Nat. Mater.* **8**, 931 (2009).
- [3] J. Zhu, J. Christensen, J. Jung, L. Martin-Moreno, X. Yin, L. Fok, X. Zhang, and F. J. Garcia-Vidal, *Nat. Phys.* **7**, 52 (2011).
- [4] S. Zhang, C. Xia, and N. Fang, *Phys. Rev. Lett.* **106**, 024301 (2011).
- [5] B.-I. Popa, L. Zigoneanu, and S. A. Cummer, *Phys. Rev. Lett.* **106**, 253901 (2011).
- [6] M. Farhat, S. Enoch, S. Guenneau, and A. B. Movchan, *Phys. Rev. Lett.* **101**, 134501 (2008).
- [7] M. Farhat, S. Guenneau, and S. Enoch, *Phys. Rev. Lett.* **103**, 024301 (2009).
- [8] N. Stenger, M. Wilhelm, and M. Wegener, *Phys. Rev. Lett.* **108**, 014301 (2012).
- [9] B. Popa and S. A. Cummer, *Nat. Commun.* **5**, 3398 (2014).
- [10] R. Li, X. Zhu, B. Liang, Y. Li, X. Zou, and J. Cheng, *Appl. Phys. Lett.* **99**, 193507 (2011).
- [11] A. Climente, D. Torrent, and J. Sánchez-Dehesa, *Appl. Phys. Lett.* **100**, 144103 (2012).
- [12] J. Mei, G. Ma, M. Yang, Z. Yang, W. Wen, and P. Sheng, *Nat. Commun.* **3**, 756 (2012).
- [13] J. Z. Song, P. Bai, Z. H. Hang, and Y. Lai, *New J. Phys.* **16**, 033026 (2014).
- [14] X. Ni, C. He, X. Sun, X. Liu, M. Lu, L. Feng, and Y. Chen, *New J. Phys.* **17**, 053016 (2015).
- [15] Z. Yang, F. Gao, X. Shi, X. Lin, Z. Gao, Y. Chong, and B. Zhang, *Phys. Rev. Lett.* **114**, 114301 (2015).
- [16] P. Wang, L. Lu, and K. Bertoldi, *Phys. Rev. Lett.* **115**, 104302 (2015).
- [17] Z.-G. Chen and Y. Wu, *Phys. Rev. Appl.* **5**, 054021 (2016).
- [18] A. B. Khanikaev, R. Fleury, S. H. Mousavi, and A. Alù, *Nat. Commun.* **6**, 8260 (2015).
- [19] L. M. Nash, D. Kleckner, A. Read, V. Vitelli, A. M. Turner, and T. M. Irvine, *Proc. Natl. Acad. Sci. (USA)* **112**, 14495 (2015).
- [20] Z. Liu, X. Zhang, Y. Mao, Y. Y. Zhu, Z. Yang, C. T. Chan, and P. Sheng, *Science* **289**, 1734 (2000).
- [21] Z. Liu, C. T. Chan, and P. Sheng, *Phys. Rev. B* **71**, 014103 (2005).
- [22] N. Fang, D. Xi, J. Xu, M. Ambati, W. Srituravanich, C. Sun, and X. Zhang, *Nat. Mater.* **5**, 452 (2006).
- [23] Y. Ding, Z. Liu, C. Qiu, and J. Shi, *Phys. Rev. Lett.* **99**, 093904 (2007).
- [24] Y. Wu, Y. Lai, and Z. Q. Zhang, *Phys. Rev. Lett.* **107**, 105506 (2011).
- [25] M. Yang, G. Ma, Z. Yang, and P. Sheng, *Phys. Rev. Lett.* **110**, 134301 (2013).
- [26] J. Li and C. T. Chan, *Phys. Rev. E* **70**, 055602(R) (2004).
- [27] D. Censor and J. Aboudi, *J. Sound Vib.* **19**, 437 (1971).
- [28] R. Fleury, D. L. Sounas, C. F. Sieck, M. R. Haberman, and A. Alù, *Science* **343**, 516 (2014).
- [29] Q. Wang, Y. Yang, X. Ni, Y. Xu, X. Sun, Z. Chen, L. Feng, X. Liu, M. Lu, and Y. Chen, *Sci. Rep.* **5**, 10880 (2015).
- [30] A. M. Mahmoud, A. R. Davoyan, and N. Engheta, *Nat. Commun.* **6**, 8359 (2015).
- [31] Z. Liu, C. T. Chan, and P. Sheng, A. L. Goertzen, and J. H. Page, *Phys. Rev. B* **62**, 2446 (2000).
- [32] J. Mei, Z. Liu, J. Shi, and D. Tian, *Phys. Rev. B* **67**, 245107 (2003).
- [33] Y. Wu, J. Li, Z. Q. Zhang, and C. T. Chan, *Phys. Rev. B* **74**, 085111 (2006).
- [34] D. M. Pozar, *Microwave Engineering* (Wiley, New York, 1998).
- [35] P. Y. Chen, C. G. Poulton, A. A. Asatryan, M. J. Steel, L. C. Botten, C. Martijn de Sterke, and R. C. McPhedran, *New J. Phys.* **13**, 053007 (2011).
- [36] P. Markoš and R. Hlubina, *Phys. Lett. A* **380**, 811 (2016).
- [37] O. Toader and S. John, *Phys. Rev. E* **70**, 046605 (2004).
- [38] D. Hermann, M. Diem, S. F. Mingaleev, A. García-Martín, P. Wölflle, and K. Busch, *Phys. Rev. B* **77**, 035112 (2008).
- [39] N. Wang, Z. Q. Zhang, and C. T. Chan, *Phys. Rev. B* **98**, 085142 (2018).
- [40] M. J. A. Smith and P. Y. Chen, *Phys. Rev. Lett.* **121**, 103902 (2018).

- [41] A. A. Zyablovsky, A. P. Vinogradov, A. V. Dorofeenko, A. A. Pukhov, and A. A. Lisyansky, *Phys. Rev. A* **89**, 033808 (2014).
- [42] M. Lavery, F. Speirits, S. Barnett, and M. Padgett, *Science* **341**, 537 (2013).
- [43] K. Ding, Z. Q. Zhang, and C. T. Chan, *Phys. Rev. B* **92**, 235310 (2015).
- [44] W. D. Heiss, *J. Phys. A* **45**, 444016 (2012).
- [45] Z. Wang, Y. D. Chong, J. D. Joannopoulos, and M. Soljačić, *Phys. Rev. Lett.* **100**, 013905 (2008).
- [46] Z. Wang, Y. D. Chong, J. D. Joannopoulos, and M. Soljačić, *Nature (London)* **461**, 772 (2009).
- [47] J. Wang, H. Y. Dong, C. W. Ling, C. T. Chan, and K. H. Fung, *Phys. Rev. B* **91**, 235410 (2015).